



DeepPhase: Learning phase contrast signal from dual energy X-ray absorption images[☆]

Ronghui Luo¹, Yongshuai Ge¹, Zhanli Hu¹, Dong Liang^{*}, Zhi-Cheng Li^{*}

Shenzhen Institute of Advanced Technology, Chinese Academy of Sciences, Shenzhen 518055, China

ARTICLE INFO

Keywords:

X-ray phase contrast imaging
Deep learning
Dual-energy imaging

ABSTRACT

Due to the high hardware complexity and low dose efficiency of existing X-ray phase contrast imaging, the biomedical and clinical applications of this novel imaging technique have been hindered. This study proposes a deep learning method, named DeepPhase, to extract differential phase contrast (DPC) image from two dual-energy absorption images. It obviates the need of dedicated DPC imaging devices such as Talbot–Lau gratings and is compatible with diagnostic-level dual-energy X-ray imaging hardware. Given two dual-energy absorption images for an object, all we need to produce its DPC image at a certain energy is a well-trained DeepPhase network. Results demonstrate that, compared with conventional Talbot–Lau interferometry, DeepPhase achieves high-quality DPC imaging at multiple dual-energy combinations and low radiation dose.

1. Introduction

Compared with traditional absorption-based X-ray imaging, X-ray phase contrast imaging (XPCI) has proven to show superior contrast performance for certain soft tissue or materials with low density and low Z, and therefore has attracted great attention for decades [1,2]. Various XPCI techniques have been developed [1–4]. Among them, the grating-based Talbot–Lau interferometry has the advantage of being compatible with conventional polychromatic incoherent X-ray tube sources, as well as the unique advantage of simultaneously acquiring three images namely absorption image, differential phase contrast (DPC) image, and dark-field image, which renders this novel imaging a promising candidate to translate into biomedical and clinical applications [5].

Despite the virtues, however, the Talbot–Lau system has a low radiation dose efficiency as more than half of photons penetrating through the object are blocked by the analyzer grating. This poses a clear barrier to its clinical application. To overcome this challenge, one potential strategy is to design a new interferometer with enhanced DPC signal, as reported in [6]. Although this new design obviates the analyzer gratings, the need for submicron phase gratings adds further difficulty in grating fabrication. An alternative strategy is to increase the dose efficiency via advanced signal processing algorithms, such as the improved phase-stepping algorithms incorporated with an energy

resolving photon counting detector [7]. However, these algorithms may become invalid for conventional detectors.

Recently, the deep learning technique has shown great potential in optical imaging areas, such as ghost imaging [8], phase imaging [9], low count coherent modulation imaging [10], and super-resolution microscopy [11]. However, little work has been done in exploiting the potential of deep learning in XPCI area. Our previous studies have shown that in standard Talbot–Lau settings, deep convolutional neural network (CNN)-based DPC extraction method achieves higher accuracy with reduced noise compared with traditional phase-stepping analytical approach [12,13]. We further demonstrated that CNN-based DPC retrieval can realize high-quality single-shot Talbot–Lau imaging [14]. Although promising, these dedicated deep learning algorithms still rely on the grating-based Talbot–Lau interferometer, which can only work ideally at a fixed X-ray energy. In other words, for a given X-ray energy, placing the phase grating in other positions or even changing the tube voltage will cause DPC image acquisition failure. Obviously, this is less flexible in practical deployment.

Therefore, we propose a grating-free CNN-based DeepPhase network for learning DPC signal directly from dual-energy absorption images, which does not require the Talbot–Lau system and is compatible with current medical-level dual-energy X-ray imaging hardware. Given two dual-energy absorption images for an object, all we need to produce its DPC image at a certain energy is only a well-trained DeepPhase

[☆] This paper was recommended for publication by G. Guangtao Zhai.

^{*} Corresponding authors.

E-mail addresses: 1101533598@qq.com (R. Luo), ys.ge@siat.ac.cn (Y. Ge), zl.hu@siat.ac.cn (Z. Hu), dong.liang@siat.ac.cn (D. Liang), zc.li@siat.ac.cn (Z.-C. Li).

¹ These authors contributed equally to this work.

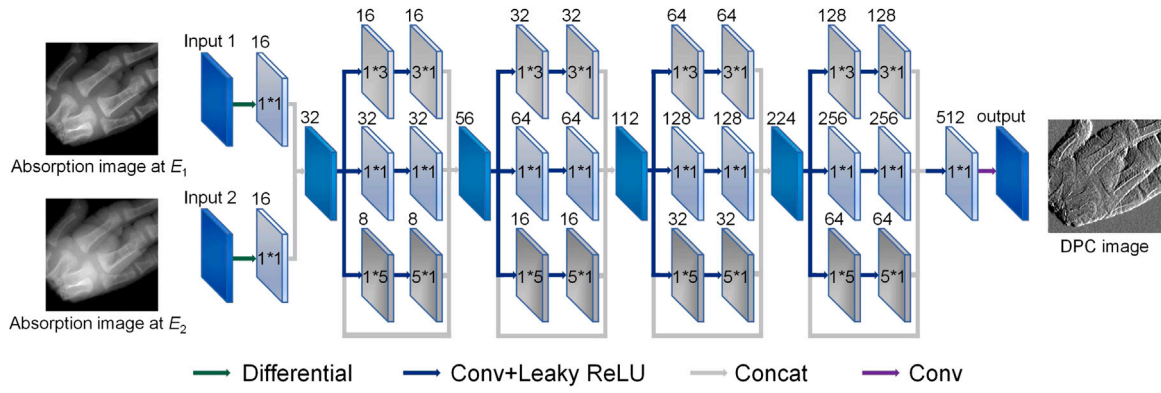


Fig. 1. Architecture of the proposed DeepPhase network. The number of channels for each convolution operation is shown.

network. These properties are made possible through the following contributions:

(1) We establish the physical basis of the DeepPhase model by deriving the mathematical relationship between the phase shift and the linear absorption coefficient, based on which we derive the nonlinear mapping from dual-energy absorption images to DPC image.

(2) We present a DeepPhase network that can efficiently learn the above mathematical relationship from synthesized imaging data in an end-to-end way. The trained DeepPhase network has been validated on simulated data, a self-developed phantom and five biological specimens.

2. Materials and methods

2.1. Physical basis of the DeepPhase

First, we aim to derive the relationship between phase shift signal and dual-energy absorption coefficients. The interaction between an X-ray and an object can be described by the object refractive index n as $n = 1 - \delta + i\beta$ [15], where the real part δ denotes the phase shift while the imaginary part β represents the absorption and is proportional to the linear absorption coefficient (intensity loss per unit path length) μ by $\mu = 4\pi\beta/\lambda$. Here λ is the wavelength.

For diagnostic X-ray imaging, μ at a certain energy E is determined by the photoelectric cross section σ_{pe} and the scattering cross section σ_{sc} as $\mu = \rho_e(\sigma_{pe} + \sigma_{sc})/Z_{eff}$, where ρ_e and Z_{eff} are the electron density and equivalent atomic number of the object, respectively. Here E denotes the effective energy of the diagnostic chromatic X-ray source spectrum (10–140 keV). Approximately, it can be considered equal to the mean beam energy. σ_{pe} can be approximated as $\sigma_{pe} = K \cdot Z_{eff}^{m-1}/E^3$, where K and m are constants [16,17]. σ_{sc} can be approximated as $\sigma_{sc} = Z_{eff} \cdot \sigma_{kn}(E)$, where $\sigma_{kn}(E)$ is the Klein–Nishina cross section [17]. Then, μ at certain energy E can be described as

$$\mu = \rho_e \cdot \left[\frac{K \cdot Z_{eff}^{m-1}}{E^3} + \sigma_{kn}(E) \right]. \quad (1)$$

Thusly, the absorption term μ at certain energy E is determined by both electron density ρ_e and equivalent atomic number Z_{eff} .

On the other hand, the phase shift term δ for certain energy E depends only on the electron density ρ_e as

$$\delta = \frac{\rho_e r_0 \hbar^2 c^2}{2\pi E^2}, \quad (2)$$

where $r_0 = 2.82 \times 10^{-15}$ m is the classical radius of the electron, \hbar is the reduced Planck constant, and c is the speed of light [17].

In Eq. (1), given μ we still have two unknown terms ρ_e and Z_{eff} . Therefore, we consider solving ρ_e from a dual-energy scan of the object. Let μ_1 and μ_2 denote the absorption coefficients of the object at two

different X-ray energies E_1 and E_2 , respectively. Based on Eq. (1), ρ_e can be calculated as

$$\rho_e = \frac{\mu_1 E_1^3 - \mu_2 E_2^3}{\theta(E_1, E_2)}, \quad (3)$$

where $\theta(E_1, E_2) = E_1^3 \sigma_{kn}(E_1) - E_2^3 \sigma_{kn}(E_2)$. Note that the term E hereafter is the equivalent energy of the phase contrast imaging while E_1, E_2 correspond to the two equivalent energies for absorption imaging.

Substituting Eq. (3) into Eq. (2), the phase shift signal δ for certain E can be expressed as a function of the dual-energy absorption coefficients μ_1 and μ_2 as

$$\delta = \mu_1 \cdot s(E_1, E_2) + \mu_2 \cdot t(E_1, E_2), \quad (4)$$

$$\text{where } s(E_1, E_2) = \frac{r_0 \hbar^2 c^2 E_1^3}{2\pi E^2 \theta(E_1, E_2)}, \quad t(E_1, E_2) = -\frac{r_0 \hbar^2 c^2 E_2^3}{2\pi E^2 \theta(E_1, E_2)}.$$

According to the Lambert–Beer law [18], the absorption image I_a can be calculated as $I_a = I_0 e^{-\int \mu dl}$, where I_0 is the total number of photons and l is the X-ray path through the object. The DPC image I_p can be defined as the derivative of the phase signal along the horizontal x direction by $I_p = \frac{2\pi}{\lambda} \frac{\partial \delta}{\partial x}$ [15]. Replacing δ as Eq. (4), the DPC image I_p can then be expressed by two dual-energy absorption images as

$$I_p = p(E_1, E_2) \frac{\partial \ln I_{a1}}{\partial x} + q(E_1, E_2) \frac{\partial \ln I_{a2}}{\partial x}, \quad (5)$$

where I_{a1} and I_{a2} represent the two dual-energy absorption images acquired at E_1 and E_2 , respectively; $p(E_1, E_2) = -\frac{2\pi}{\lambda} s(E_1, E_2)$ and $q(E_1, E_2) = -\frac{2\pi}{\lambda} t(E_1, E_2)$. The two energy-related terms $p(E_1, E_2)$ and $q(E_1, E_2)$ are independent of the object and can be considered as constants given an ideal dual-energy scan. In theory, I_p can be calculated from the dual-energy images according to Eq. (5). However, since the actual X-ray source is polychromatic, it is difficult to obtain the precise expression of $p(E_1, E_2)$ and $q(E_1, E_2)$ in Eq. (5) in practice. Given a polychromatic X-ray source, the relationship between the DPC signal I_p and the dual-energy absorption images I_{a1} and I_{a2} are highly nonlinear. Here we attempt to solve this problem by learning Eq. (5) from I_{a1} and I_{a2} using a CNN from training data.

2.2. The proposed DeepPhase model

Mathematically, every layer of the CNN performs a convolutional procedure that can be formulated as $\varphi_i = f_i(w_i * \varphi_{i-1} + b_i)$, where φ_i and φ_{i-1} represent the output and input of that layer, respectively; w_i is the convolution weight and b_i is the bias; f_i is the activation function and $*$ denotes the convolution operation. Eq. (5) can then be expressed as

$$I_p^{CNN} = f_n(w_n * f_{n-1}(\dots (w_2 * f_1(w_1 * \left[\frac{\partial \ln I_{a1}}{\partial x} \right] + b_1) + b_2) \dots) + b_n), \quad (6)$$

Table 1

Evaluation of the DPC images for the phantom and five biological specimens learned by the proposed DeepPhase at different energy combinations. The DPC image obtained by phase-stepping method on our Talbot-Lau system is used as reference in calculating the PSNR and SSIM values.

Samples	Metrics	40/60 kV	40/70 kV	40/80 kV	60/70 kV	60/80 kV	70/80 kV
Phantom	PSNR	28.59	28.23	28.16	26.86	27.15	27.97
	SSIM	0.912	0.917	0.913	0.919	0.918	0.915
Chicken claw	PSNR	31.88	32.30	33.17	27.64	31.74	31.81
	SSIM	0.925	0.924	0.922	0.929	0.930	0.927
Bullfrog forefoot	PSNR	31.88	30.35	30.23	31.03	31.64	28.87
	SSIM	0.944	0.933	0.925	0.923	0.914	0.909
Pond loach	PSNR	30.48	28.97	31.48	28.98	33.32	32.16
	SSIM	0.942	0.929	0.905	0.906	0.887	0.884
Fish tail	PSNR	30.50	29.98	29.51	30.03	30.06	28.83
	SSIM	0.925	0.924	0.919	0.935	0.932	0.933
Peascod	PSNR	33.43	31.79	32.25	29.97	30.66	31.37
	SSIM	0.921	0.915	0.879	0.869	0.829	0.831



Fig. 2. Results of numerical validation. From left to right: original image downloaded from ImageNet; two simulated dual-energy absorption images at 40 kV and 70 kV; simulated DPC image; DeepPhase-learned DPC image.

where n is the number of layers. The signals estimated by CNN are all parameterized variables with learnable w_i, b_i .

To learn the DPC signal from dual-energy absorption images, a deep CNN named DeepPhase is proposed, as illustrated in Fig. 1. It takes the unidirectional gradient of two dual-energy absorption images as input while generates a DPC image at the output end. The main body of DeepPhase consists of four cascaded phase extraction blocks. Each block has three paralleled sub-paths, including a pixel mapping sub-path and two neighborhood effect sub-paths. The pixel mapping sub-path comprises two cascaded 1×1 convolutions that learn a pixel-to-pixel transformation of the contrast information. The neighborhood effect sub-path, consisting of a 1×3 convolution followed by a 3×1 convolution, or a 1×5 convolution followed by a 5×1 convolution, is applied to account for the influence of neighboring pixels on the DPC signal transformation. Mean square error between the output image and reference is used as loss function.

To train the DeepPhase network, a large volume of labeled data, namely dual-energy absorption images and corresponding DPC image for numerous samples, is required. However, it is difficult to collect enough such data in real world. Instead, we can numerically synthesize the training data based on a well-defined physical model. We develop a numerical model that can simulate dual-energy absorption images and their corresponding DPC image for a given sample. The images downloaded from the ImageNet [19] are used to synthesize the training data. Specifically, the central region of the gray-scale converted image from ImageNet, denoted as I_m , is first resized into 256×256 . Then, the absorption images I_a and the DPC image I_p can be simulated respectively as

$$I_a = \sum_i I_0(E_i) e^{-\mu_m(E_i) \rho I_m / 256}, \quad (7)$$

$$I_p = \sum_i I_0(E_i) \frac{\partial(\rho_e I_m / 256)}{\partial u}, \quad (8)$$

where $I_0(E_i)$ is the number of photons at energy E_i (E_i ranges from 0 to 40 keV and from 0 to 70 keV for low- and high-energy imaging, respectively; E_i for DPC imaging ranges from 0 to 40 keV), $\mu_m(E_i)$ is the linear absorption coefficient at energy E_i , and ρ is the object density.

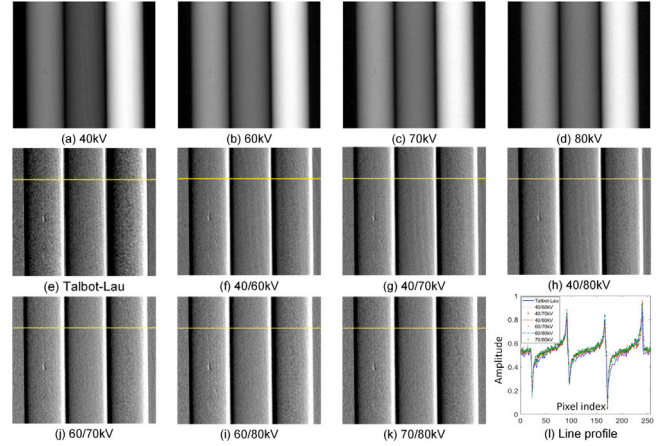


Fig. 3. Results of the phantom test. (a)–(d): absorption images obtained at 40 kV, 60 kV, 70 kV and 80 kV, respectively; (e): DPC image obtained on the Talbot-Lau interferometer at 40 kV; (f)–(k): DPC images learned by DeepPhase from dual-energy absorption image pairs obtained at 40/60 kV, 40/70 kV, 40/80 kV, 60/70 kV, 60/80 kV, and 70/80 kV, respectively. The highlighted horizontal lines are used to measure line profiles as shown in (l).

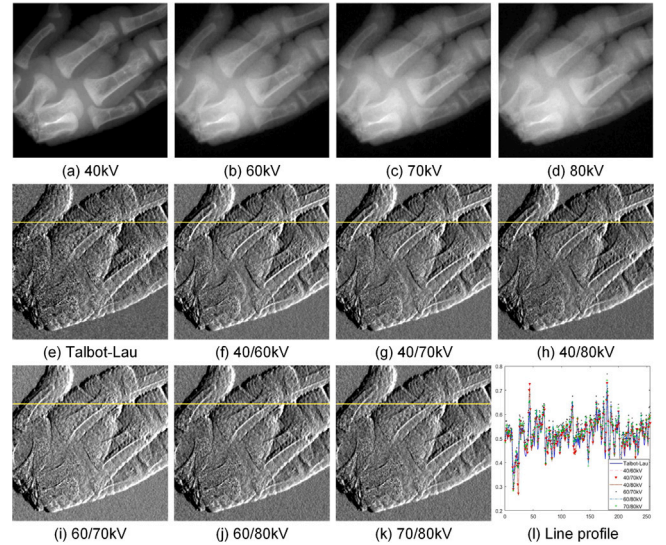


Fig. 4. Results of the chicken claw test. (a)–(d): absorption images obtained at 40 kV, 60 kV, 70 kV and 80 kV, respectively; (e): DPC image obtained on the Talbot-Lau interferometer at 40 kV; (f)–(k): DPC images learned by DeepPhase from dual-energy absorption image pairs obtained at 40/60 kV, 40/70 kV, 40/80 kV, 60/70 kV, 60/80 kV, and 70/80 kV, respectively. The highlighted lines in (e–k) are used to measure line profiles as shown in (l).

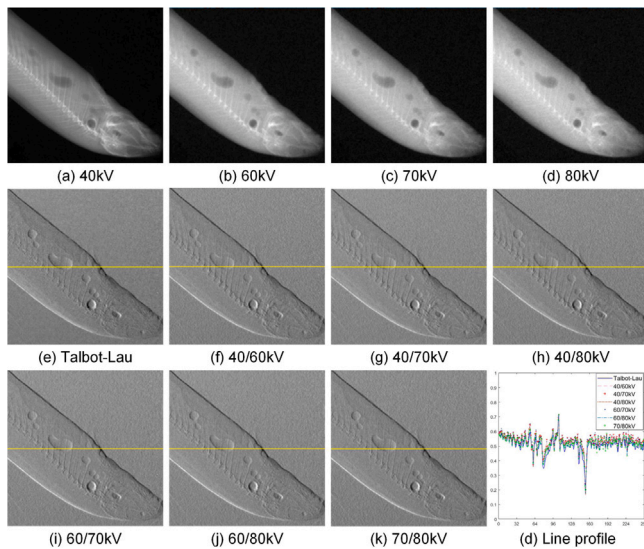


Fig. 5. Results of the pond loach test. (a)–(d): absorption images obtained at 40 kV, 60 kV, 70 kV and 80 kV, respectively; (e): DPC image obtained on the Talbot–Lau interferometer at 40 kV; (f)–(k): DPC images learned by DeepPhase from dual-energy absorption image pairs obtained at 40/60 kV, 40/70 kV, 40/80 kV, 60/70 kV, 60/80 kV, and 70/80 kV, respectively. The highlighted lines in (e–k) are used to measure line profiles as shown in (l).

In our study, $I_0(E_i)$ was simulated by the SpekCalc tool that calculates photon spectra from tungsten anode X-ray tubes [20], while $\mu(E_i)$ was obtained from the X-ray Optics utilities (XOP) that contain a database for optical and atomic constants [21]. ρ and ρ_e were obtained from the National Institute of Standards and Technology (NIST) database [22]. Finally, 60 000 dual-energy images with Poisson noise and 30 000 corresponding DPC images were simulated based on 30 000 images from ImageNet. These images were used to train a DeepPhase network. Adam optimizer was used and batch size was 32. The learning rate started at 0.0001 and exponentially decayed by a factor of 0.90 after every 50 epochs. The network was trained with 500 epochs on the TensorFlow framework using a NVIDIA Tesla V100 GPU (see loss curve in supplementary Fig.S1).

2.3. Experimental design

The DeepPhase method was demonstrated via a numerical validation on simulated images, a phantom test, and five biological specimen experiments on a fresh chicken claw, a fish tail, a bullfrog forefoot, a peascod, and a pond loach, respectively. For numerical validation, 20 000 simulated dual-energy images were used as network input and corresponding 10 000 simulated DPC images were used as reference.

In both phantom and biological specimen tests, the reference DPC images were acquired on our inhouse Talbot–Lau interferometer, including a source grating G0, a π -phase grating G1, and an analyzer grating G2, with the periods of 24.00 μm , 4.36 μm and 2.40 μm , respectively. The distances between G0 and G1, and between G1 and G2 were 1773.60 mm and 177.36 mm, respectively. A rotating-anode Tungsten target diagnostic-level tube was operated at 40 kV with a mean energy of 28 keV. A flat-panel detector with 74.8 $\mu\text{m} \times 74.8 \mu\text{m}$ resolution was used. The average fringe visibility was 0.15. The DPC image acquired by the phase-stepping analytical approach with stepping number of 8 was used as reference. When acquiring dual-energy absorption images for phantom or specimen, all three gratings were removed while the positions of the tube, detector and samples stayed unchanged. Four absorption images were acquired for each sample at 40 kV, 60 kV, 70 kV, and 80 kV, respectively. Two of them were used as network input.

The difference between the learned image and the reference was assessed using both peak signal-to-noise ratio (PSNR) and structural

similarity index metric (SSIM). All images were Z-score normalized, based on which the line profiles were measured to assess the learned images. When calculating PSNR and SSIM, the simulated DPC images were used as reference for numerical validation while the experimental DPC images obtained on our Talbot–Lau system were used as reference for both phantom and biological specimen tests.

3. Results

3.1. Numerical validation

An example of the numerical validation results is shown in Fig. 2. It shows that DeepPhase can learn almost equivalent DPC image as of the conventional phase-stepping images obtained at the Talbot–Lau interferometer. The average PSNR and SSIM over all numerical validation samples are 32.10 and 0.95, respectively (see PSNR and SSIM distribution over validation samples in supplementary Fig.S2). The results initially validate the feasibility of the DeepPhase network in learning DPC images from dual-energy absorption images.

3.2. Phantom test

The self-developed phantom comprises three cylinders made of different plastic materials: POM, GPPS and PTFE. The results of the phantom study are shown in Fig. 3, where the line profiles are provided for assessing the learned images. The PSNR and SSIM was summarized in Table 1, where the numbers (e.g. 40/60 kV) in the first row represents the low and high voltages in acquiring dual-energy images. The results demonstrate that DeepPhase can learn DPC images accurately at multiple energy combinations, even when the energies for the absorption and DPC imaging are totally different. In the learned images, a flaw inside the left cylinder is well preserved while the noise induced by the phase-stepping procedure decreases. Visually, no significant difference can be observed in the DeepPhase-generated images learned from absorption image pairs acquired at different energy combinations, although the PSNRs are slightly higher when an absorption image acquired at 40 kV was used.

3.3. Biological specimen experiment

The experimental results of the chicken claw specimen and the pond loach are shown in Fig. 4 and Fig. 5, respectively (see results of the other three biological specimens, including fish tail, bullfrog forefoot, and peascod, in supplementary Fig.S3–S5). Table 1 summarizes the PSNR and SSIM of the five tested biological specimens. Similarly, the results show that DeepPhase can accurately learn DPC images with good spatial detail preservation at all tested energy combinations. Particularly, one can observe that the learned images in Fig. 4(f–k) depicted the bone structures within the claw better compared with the phase-stepping image in (e). This may be due to the fact that for phase-stepping imaging, strong dark-field signals generated by the bones will enhance the uncertainties of the DPC signal and therefore cause higher noise. This observation is consistent with phantom findings, and hence further validates the feasibility of DeepPhase in learning accurate phase signals from synthesized training data.

3.4. Dose effect

The effect of radiation dose on the chicken claw DPC imaging was analyzed. Exposure time of 2.5s, 5s, 7.5s and 10 s were used with corresponding dose level of 25%, 50%, 75% and 100%, respectively. Fig. 6 shows the DPC images obtained by both Talbot–Lau system and DeepPhase method at these dose levels. We observe that DPC images acquired on the Talbot–Lau system contain stronger noise than those learned by DeepPhase, especially for the bony structures within the claw. The effect becomes more serious when the dose decreases, as

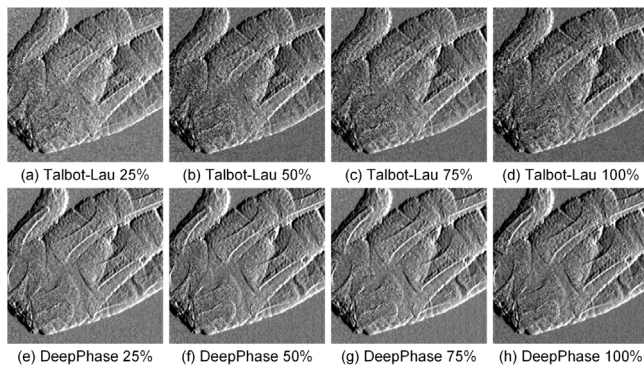


Fig. 6. Comparison of DPC images obtained by Talbot-Lau interferometry and DeepPhase at different radiation dose levels. (a)–(d): DPC images obtained on the Talbot-Lau interferometer at 40 kV with 25%, 50%, 75% and 100% dose levels, respectively; (e)–(h): DPC images generated by DeepPhase learned from dual-energy absorption image pair at 40/60 kV with 25%, 50%, 75% and 100% dose levels, respectively.

Table 2
Evaluation of the DPC images learned by the proposed DeepPhase at different radiation dose levels.

Metrics	Methods	25%	50%	75%
PSNR	Talbot-Lau	26.07	30.22	30.23
	DeepPhase	29.62	32.26	32.57
SSIM	Talbot-Lau	0.746	0.761	0.770
	DeepPhase	0.836	0.850	0.856

shown by the PSNR and SSIM listed in Table 2. For the DeepPhase learned DPC images, the spatial details especially the bony structures can be better exhibited at the same dose level. Visually, the DeepPhase learned DPC image acquired at 25% dose exhibits comparable quality as that acquired at 100% dose. When comparing the DeepPhase image (e) acquired at 25% dose with the Talbot-Lau image (d) acquired at 100% dose, the former depicts object details better than the latter (see the claw bony structures). This is an important observation as it indicates that, although the DeepPhase requires two exposures to obtain dual-energy images for an object, the total dose needed for the same image quality could still be lower than the Talbot-Lau method.

4. Discussion and conclusions

The object of this study is to develop and validate a deep CNN model, named DeepPhase, which learns an X-ray DPC image from two dual-energy absorption images. The main findings of the study include: (1) DeepPhase can learn the relationship between dual-energy absorption images and DPC image from synthesized imaging data downloaded from ImageNet; (2) The learned DPC images have similar quality in terms of PSNR and SSIM compared with the DPC images acquired using phase-stepping method on Talbot-Lau interferometry.

Our DeepPhase method is based on a well-defined physical model that described the mathematical relationship between the phase shift signal and the dual-energy absorption coefficients. According to our model, the relationship between the DPC image and the dual-energy images are a pixel-to-pixel mapping, as summarized in Eq. (5). Our DeepPhase model is designed to learn this pixel mapping between the dual-energy absorption images and the DPC image, rather than to mimic a plausible DPC-like image by image-level or object-level edge detection or Generative Adversarial Networks (GAN)-like image synthesis techniques. From the viewpoint of supervised machine learning, a well-trained CNN model learns a function that optimally maps input to output based on labeled input-output pairs, and the inferred function can be used for mapping new samples. In our study, the training pairs include two dual-energy absorption images as input, and one corresponding DPC image as output. In theory, DeepPhase can use any type

of image pair for training, as long as the image pair used for training conforms to the mathematical relationship mapping from dual-energy images to DPC image. In other words, the accuracy of DeepPhase is independent of the image-level content (animals, human, cars, etc.) of the training images, but relies on the pixel-wise relationship between image pair used for training.

The performance of the proposed DeepPhase model has been comprehensively demonstrated via a numerical validation on simulated images, a phantom test, and five biological specimen experiments, as shown in the results section and in online supplementary materials. The PSNR and SSIM results show that the learned DPC image has almost equivalent quality compared with the real DPC image acquired using phase-stepping method on Talbot-Lau interferometry. Furthermore, DeepPhase can generate similar images from dual-energy images obtained at different energy combination. On the other hand, our results show that although DeepPhase model requires two exposures to obtain dual-energy absorption images, the radiation dose not significantly increase: the model has comparable performance at low-dose conditions.

Herein, we would like to point out the limitations of our study. First, DeepPhase is developed for biomedical scenarios with a diagnostic-level energy range, where the absorption edge effect can be ignored and Z_{eff} can be seen as energy independent. Second, according to the physical basis shown in Eqs. (4) and (5), our model learns the DPC signal from the difference between two absorption images obtained at different energies. In other words, the absorption coefficients μ_1 and μ_2 of an object for the dual-energy scan should be different. Otherwise, if μ_1 and μ_2 are the same, the problem becomes underdetermined and cannot be solved properly. Therefore, our model may fail in the extreme situation of a sample having the same absorption coefficients but different phase shifts. However, in practice such situation seldom occurs. Generally, if the absorption coefficients of two objects at different energies are exactly the same, these two objects are most likely made of the same material. Furthermore, we would like to emphasize that the proposed learning model cannot replace the Talbot-Lau method or other imaging devices, but offers an opportunity to generate the DPC image in certain conditions. For example, if Talbot-Lau hardware is unavailable while dual-energy system is available, the DPC image can be produced by using our method to offer more information of interest.

In conclusion, this paper for the first time demonstrates the feasibility of extracting DPC image from dual-energy absorption images using deep learning, avoiding the dependence of conventional XPCI devices such as gratings-based Talbot-Lau interferometer. Experimental results validate that the proposed DeepPhase has great potential to improve image quality and preserve spatial details with reduced noise. In future we will further validate the DeepPhase on animals and human data.

CRedit authorship contribution statement

Ronghui Luo: Methodology, Software, Validation, Formal analysis, Writing - original draft. **Yongshuai Ge:** Methodology, Data curation, Resources, Funding acquisition. **Zhanli Hu:** Methodology, Resources. **Dong Liang:** Resources, Conceptualization. **Zhi-Cheng Li:** Writing - original draft, Supervision.

Declaration of competing interest

The authors declare that they have no known competing financial interests or personal relationships that could have appeared to influence the work reported in this paper.

Acknowledgments

This work was supported by Shenzhen Fundamental Research Program, China (JCYJ20170413162354654), National Natural Science Foundation of China (12027812, 11804356), and Youth Innovation Promotion Association of Chinese Academy of Sciences (2018364, 2021362).

Appendix A. Supplementary data

Supplementary material related to this article can be found online at <https://doi.org/10.1016/j.displa.2021.102027>.

References

- [1] A. Momose, T. Takeda, Y. Itai, K. Hirano, Phase-contrast X-ray computed tomography for observing biological soft tissues, *Nature Med.* 2 (4) (1996) 473–475.
- [2] F. Pfeiffer, T. Weitkamp, O. Bunk, C. David, Phase retrieval and differential phase-contrast imaging with low-brilliance X-ray sources, *Nat. Phys.* 2 (4) (2006) 258–261.
- [3] T.J. Davis, T.E. Gureyev, A.W. Stevenson, S.W. Wilkins, D. Gao, Phase-contrast imaging of weakly absorbing materials using hard X-rays, *Nature* 373 (6515) (1995) 595–598.
- [4] C. David, B. Nöhammer, H.H. Solak, E. Ziegler, Differential X-ray phase contrast imaging using a shearing interferometer, *Appl. Phys. Lett.* 81 (17) (2002) 3287–3289.
- [5] Z. Wang, N. Hauser, G. Singer, M. Trippel, M. Stampanoni, Non-invasive classification of microcalcifications with phase-contrast X-ray mammography, *Nature Commun.* 5 (3797) (2014).
- [6] H. Miao, A. Panna, A.A. Gomella, E.E. Bennett, S. Znati, L. Chen, H. Wen, A universal moiré effect and application in X-ray phase-contrast imaging, *Nat. Phys.* 12 (9) (2016) 830–834.
- [7] Y. Ge, R. Zhang, K. Li, G.-H. Chen, Improving radiation dose efficiency of X-ray differential phase contrast imaging using an energy-resolving grating interferometer and a novel rank constraint, *Opt. Express* 24 (12) (2016) 12955–12968.
- [8] F. Wang, H. Wang, H. Wang, G. Li, G. Situ, Learning from simulation: An end-to-end deep-learning approach for computational ghost imaging, *Opt. Express* 27 (18) (2019) 25560–25572.
- [9] S. Feng, Q. Chen, G. Gu, T. Tao, L. Zhang, Y. Hu, W. Yin, C. Zuo, Fringe pattern analysis using deep learning, *Adv. Photonics* 1 (3) (2019) 025001.
- [10] I. Kang, F. Zhang, G. Barbastathis, Phase extraction neural network (PhENN) with coherent modulation imaging (CMI) for phase retrieval at low photon counts, *Opt. Express* 28 (15) (2020) 21578–21600.
- [11] A. Durand, T. Wiesner, M.-A. Gardner, L. Émile Robitaille, A. Bilodeau, C. Gagné, P.D. Koninck, F. Lavoie-Cardinal, A machine learning approach for online automated optimization of super-resolution optical microscopy, *Nature Commun.* 9 (5247) (2018).
- [12] Y. Ge, P. Liu, Y. Ni, J. Chen, J. Yang, T. Su, H. Zhang, J. Guo, H. Zheng, Z.-C. Li, D. Liang, Enhancing the X-ray differential phase contrast image quality with deep learning technique, *IEEE Trans. Biomed. Eng.* (2020) <http://dx.doi.org/10.1109/TBME.2020.3011119>.
- [13] J. Chen, J. Zhu, Z. Li, W. Shi, Q. Zhang, Z. Hu, H. Zheng, D. Liang, Y. Ge, Automatic image-domain Moiré artifact reduction method in grating-based X-ray interferometry imaging, *Phys. Med. Biol.* 64 (19) (2019).
- [14] P. Liu, J. Yang, J. Chen, T. Su, Y. Ge, Model-driven phase retrieval network for single-shot X-ray Talbot–Lau interferometer imaging, *Opt. Lett.* 45 (22) (2020) 6314–6317.
- [15] R.A. Lewis, Medical phase contrast X-ray imaging: current status and future prospects, *Phys. Med. Biol.* 49 (16) (2004) 3573.
- [16] J.M. Boone, A.E. Chavez, Comparison of X-ray cross sections for diagnostic and therapeutic medical physics, *Med. Phys.* 23 (12) (1996) 1997–2005.
- [17] Z. Qi, J. Zambelli, N. Bevins, G.H. Chen, Quantitative imaging of electron density and effective atomic number using phase contrast CT, *Phys. Med. Biol.* 55 (9) (2010) 2669.
- [18] G. Stokes, On the intensity of the light reflected from or transmitted through a pile of plates, *J. Opt. Soc. Amer.* 11 (10) (1947) 545–556.
- [19] O. Russakovsky, J. Deng, H. Su, J. Krause, S. Satheesh, S. Ma, Z. Huang, A. Karpathy, A. Khosla, M. Bernstein, Imagenet large scale visual recognition challenge, *Int. J. Comput. Vis.* 115 (3) (2015) 211–252.
- [20] G. Poludniowski, G. Landry, F. DeBlois, P.M. Evans, F. Verhaegen, Spekcalc: a program to calculate photon spectra from tungsten anode X-ray tubes, *Phys. Med. Biol.* 54 (19) (2009) N433.
- [21] M.S. del Río, R.J. Dejus, XOP v2.4: recent developments of the X-ray optics software toolkit, in: *Advances in Computational Methods for X-Ray Optics II*, vol. 8141, SPIE, 2011.
- [22] J.H. Hubbell, S.M. Seltzer, NIST Standard Reference Database 126, 2004, <http://dx.doi.org/10.18434/T4D01F>.